

# Efficient Photoelectrochemical Water Splitting with Ultrathin films of Hematite on Three-Dimensional Nanophotonic Structures

Yongcai Qiu,<sup>†,‡</sup> Siu-Fung Leung,<sup>†</sup> Qianpeng Zhang,<sup>†</sup> Bo Hua,<sup>†</sup> Qingfeng Lin,<sup>†</sup> Zhanhua Wei,<sup>‡</sup> Kwong-Hoi Tsui,<sup>†</sup> Yuegang Zhang,<sup>§</sup> Shihe Yang,<sup>\*,‡</sup> and Zhiyong Fan<sup>\*,†</sup>

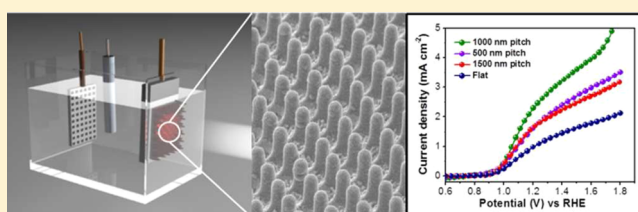
<sup>†</sup>Department of Electronic and Computer Engineering and <sup>‡</sup>Department of Chemistry, The Hong Kong University of Science and Technology, Clear Water Bay, Kowloon, Hong Kong, People's Republic of China

<sup>§</sup>i-LAB, Suzhou Institute of Nano-Tech and Nano-Bionics, Chinese Academy of Sciences, People's Republic of China

## Supporting Information

**ABSTRACT:** Photoelectrochemical (PEC) solar water splitting represents a clean and sustainable approach for hydrogen ( $H_2$ ) production and substantial research are being performed to improve the conversion efficiency. Hematite ( $\alpha\text{-Fe}_2\text{O}_3$ ) is considered as a promising candidate for PEC water splitting due to its chemical stability, appropriate band structure, and abundance. However, PEC performance based on hematite is hindered by the short hole diffusion length that put a constraint on the active layer thickness and its light absorption capability. In this work, we have designed and fabricated novel PEC device structure with ultrathin hematite film deposited on three-dimensional nanophotonic structure. In this fashion, the nanophotonic structures can largely improve the light absorption in the ultrathin active materials. In addition, they also provide large surface area to accommodate the slow surface water oxidation process. As the result, high current density of  $3.05\text{ mA cm}^{-2}$  at  $1.23\text{ V}$  with respect to the reversible hydrogen electrode (RHE) has been achieved on such nanophotonic structure, which is about three times of that for a planar photoelectrode. More importantly, our systematic analysis with experiments and modeling revealed that the design of high performance PEC devices needs to consider not only total optical absorption, but also the absorption profile in the active material, in addition to electrode surface area and carrier collection.

**KEYWORDS:** Electrochemical, water splitting, nanophotonics, hematite, nanopike



Solar-driven water splitting with photoelectrochemical (PEC) reaction is a clean and effective approach for clean fuel hydrogen ( $H_2$ ) production.<sup>1–4</sup> In general, it involves absorption of abundant sunlight with a semiconductor electrode to produce electron–hole pairs, followed by oxidation and reduction of water to generate oxygen and hydrogen fuel. Obviously, the light absorption capability of the semiconductor electrode is of crucial importance and it can largely determine the ultimate energy conversion efficiency of the process. Recently, enormous effort has been invested on exploring proper semiconductor materials for efficient PEC water splitting.<sup>5–8</sup> Among all the materials being investigated, hematite ( $\alpha\text{-Fe}_2\text{O}_3$ ) is regarded as a highly promising candidate due to its excellent stability in water and electrolyte, composition of low-cost, earth-abundant and environmentally benign elements, and more importantly, close to the ideal energy band gap ( $E_g \sim 2\text{ eV}$ ), which can absorb a large portion of solar irradiation spectrum and suitable valence band edge position.<sup>9–14</sup> However, low rate constant of water oxidation and a short hole diffusion length ( $\sim 2\text{--}4\text{ nm}$ ) in hematite<sup>15</sup> in addition to its poor conductivity result in utilization of holes only generated in the proximity of electrode/electrolyte interface, and the rest of them are lost through recombination with electrons. Therefore, various nanostructured hematite, such as nanowires,<sup>16</sup> nanotubes,<sup>17</sup> nanodendrites,<sup>14,18,19</sup> and so

forth,<sup>20–22</sup> have been fabricated to improve surface area and demonstrated improved PEC performance. Additionally, it is well-known that the rational design and construction of mesostructured or hybrid materials is one of the most effective strategies to enhance its performance.<sup>23–25</sup> Despite these progresses, we are still far from reaching the ideal photocurrent density of  $12.6\text{ mA cm}^{-2}$  with hematite photoanode<sup>13</sup> due mainly to the light absorption and carrier recombination losses. In fact, the aforementioned nanostructures typically do not have well engineered geometries and morphologies, therefore the shortened and reliable carrier transport path cannot always be achieved. In general, for an active material with short carrier diffusion length, thinning down the material can lead to the improved carrier collection.<sup>26–29</sup> However, this will obviously result in the loss of light absorption. A promising solution to this dilemma is to utilize nanophotonic structures to achieve sufficient light absorption with small amount of active material. This has been proven effective for amorphous Si and CdTe ultrathin films in recent studies.<sup>30–33</sup> In this regard, deposition of ultrathin hematite films on conductive three-dimensional

Received: January 28, 2014

Revised: February 24, 2014

(3D) nanophotonic structures has a number of conspicuous advantages. In this type of architecture, the longest carrier transport distance is the thin film thickness itself, and it is highly uniform across the entire device, unlike the aforementioned hierarchical structures. Meanwhile, 3D nanophotonic structures provide excellent light-trapping capability, ensuring sufficient light absorption with thin hematite film. In effect, this scheme can decouple the competition between optical absorption and carrier transport and leads to optically “thick” and electrically “thin” materials, which have not yet been demonstrated for PEC solar water splitting devices.

In this work, we demonstrate efficient PEC water splitting with ultrathin hematite films coated on regular arrays of 3D conductive nanospikes (NSPs). In this device structure, the purpose-built 3D architectures were utilized to harvest light efficiently, the ultrathin hematite films serve as active materials to produce photocarriers, and the conductive NSPs act as efficient carrier collection path. Essentially, the NSP PEC devices have a core/shell structure, which demonstrated improved carrier collection performance for nanostructured photovoltaic devices previously.<sup>34,35</sup> The details of device fabrication process can be described as the following. Three-dimensional NSPs were fabricated with a unique imprint nanoengineering approach in conjunction with scalable Al anodization. Also, NSP fabricated with this approach have well-controlled geometries, that is, pitch and height that allow the investigation of geometry-dependent optical absorption and device efficiency. Figure 1 demonstrates the schematics and the

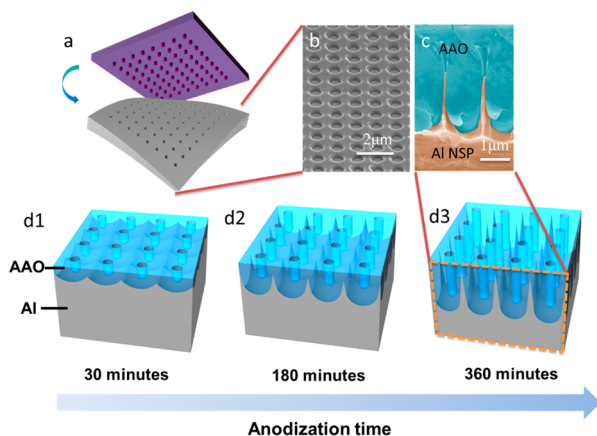


**Figure 1.** The 3D NSP array photoelectrode. (a) Schematic diagram and (b) SEM image of nanoimprint of squarely ordered nanoindentation of Al foil. (c) Cross-sectional SEM image showing Al NSP embedded in squarely order AAO. Schematic diagram showing transition of NSP height from short to tall after (d1) 30, (d2) 180, and (d3) 360 min anodization.

corresponding scanning electron microscopy (SEM) images of regular 3D NSP array fabrication. As illustrated in Figure 1a, the fabrication process started with nanoimprint of squarely ordered nanoindentation by a silicon stamp on a clean and flat Al foil to define location of the anodic aluminum oxide (AAO) pore formation by the subsequent anodization and therefore determining the pitch as well as the ordering of AAO. Figure 1b shows aluminum foil with perfect squarely ordered nanoindentation after nanoimprint. Notably, hexagonally ordered AAO is normally formed in self-organized mechanism as honeycomb structure is the most stable structure in nature. In particular, squarely ordered AAO growth will lead to the

presence of voids that will be filled by unanodized aluminum NSP. Figure 1c shows the cross-section image of an as-anodized aluminum foil with NSP underneath rendered with light brown color. In addition to the pitch, height of NSP can also be precisely controlled and it is directly related to the thickness of AAO and anodization time. Figure 1d illustrates the gradual transition of NSP height from short to tall with increasing anodization time. In the case of 30 min anodization, the AAO was found too thin to support the growth of tall NSP (Figure 1d1) and 180 min anodization lead to short NSP (Figure 1d2). Over 360 min anodization (Figure 1d3), the height of NSP was found to be saturated and the maximum height is about 110% of the NSP pitch. The formation of NSP can be further evidenced by comparing the bottom SEM views of the hexagonally and squarely ordered AAO in Supporting Information Figure S1, which shows the presence of void under the squarely order AAO and that allows formation of NSP. Perfectly ordered NSP array was obtained after removal of AAO by wet chemical etching and Figure 2a–c shows the 1000 nm pitch NSP array fabricated by 30, 180, and 360 min anodization with height of about 350, 750, and 1100 nm, respectively. For the sake of comparison, water-splitting device on NSP with pitch of 500 and 1500 nm were also fabricated (Supporting Information Figure S2) to investigate the effect of NSP pitch on optical absorption and device performance. Because the commonly used electrolyte (1 M NaOH, pH = 13.6) for Fe<sub>2</sub>O<sub>3</sub> PEC water splitting can attack the Al metal substrate, the NSP was converted to Al<sub>2</sub>O<sub>3</sub> via low voltage anodization (20 V in 3.4 wt % H<sub>2</sub>SO<sub>4</sub> for 2 h), followed by deposition of several protective coating layer, including a ~100 nm thick Ti/Pt metal layer and a ~200 nm thick fluorine-doped tin oxide (FTO) layer (detailed process flow can be found in Supporting Information Figure S3), as illustrate in Figure 2d. Note that the FTO layer was also deposited via Ultrasonic Spray Pyrolysis (USP) method using an ethanol solution of SnCl<sub>4</sub> (0.2 M) and NH<sub>4</sub>F (0.04 M) (Supporting Information Figure S4). The uniformity and conformality of each deposited layer are clearly evidenced in Supporting Information Figure S3 and S4, essentially replicating the original morphology of the NSP template. In particular, we have demonstrated that the simple USP technique is quite generic and versatile; it is suitable for depositing FTO, as well as hematite to be described immediately below, on NSP substrates. Because the intrinsic hematite has poor conductivity, Ti doping was explored in our work. For the USP deposition of Ti-doped hematite (Supporting Information Figures S5 and S6 show control experiments on glass substrates), an ethanol solution of titanium diisopropoxide bisacetylacetonate and iron trisacetylacetonate (5 mM) was used. Device performance was enhanced with increasing thickness of hematite initially due to the improved optical absorption by thicker absorber and eventually reached a peak. Further increase of hematite thickness led to decrease of device performance due to the longer carrier diffusion path than the minority carrier diffusion length and the detail can be found in Supporting Information Figure S8a. The optimized ultrathin Ti-hematite layer was found to have a thickness of ~85 nm and a Ti/Fe atom ratio of 3:35. As shown in Figure 2e, the Ti-hematite thin film on the NSP substrate is highly uniform.

To confirm the light trapping property of the NSPs, their optical properties have been characterized by UV–vis optical absorption after hematite deposition. Figure 3a shows the optical absorption spectra of the devices on NSP substrates

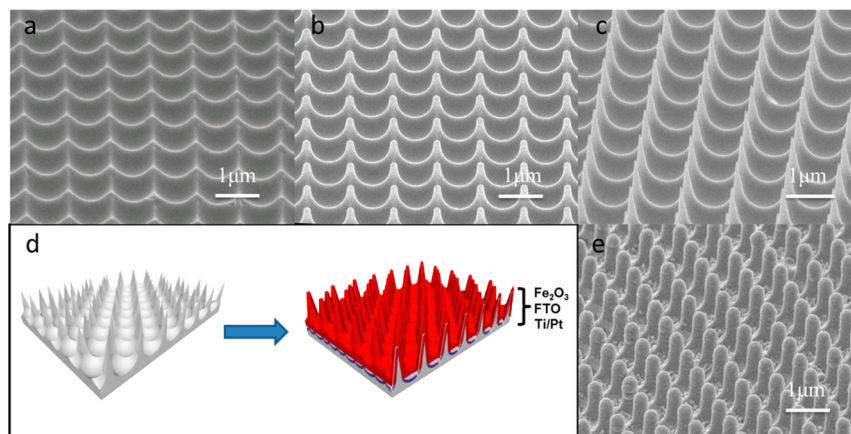


**Figure 2.** SEM images of 3D NSP photoelectrode. Sixty degree tilted SEM images of 1000 nm pitch NSP with NSP height of about (a) 350, (b) 750, and (c) 1100 nm. (d) Schematic diagram of multiple layers thin film deposition including, Ti/Pt of 100 nm, FTO of 200 nm and  $\text{Fe}_2\text{O}_3$  of 85 nm for water splitting device fabrication. (e) Sixty degree tilted SEM view of  $\text{Fe}_2\text{O}_3$  decorated NSPs.

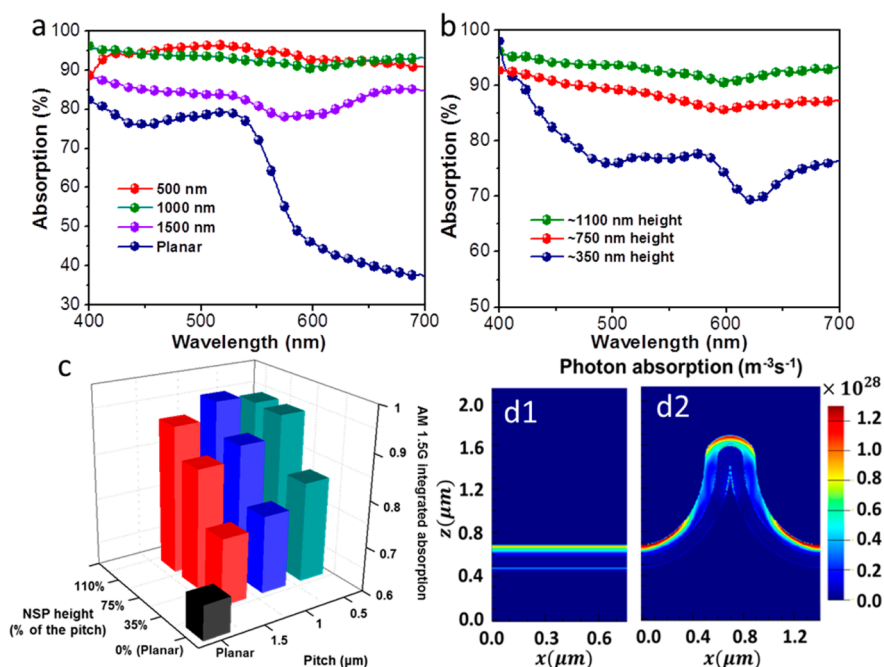


**Figure 3.** Optical absorption measurement and simulation. UV–vis optical absorption spectra of device on NSP substrate with (a) different pitches and (b) different heights in 1000 nm pitch. (c) Simulated AM1.5G spectrum integrated absorption of device with different geometry including NSP pitch and height. (d) Cross-sectional photon absorption profile of device on (d1) planar and (d2) NSP substrate. Red color hot area representing high generation indicating effective light trapping by NSP.

with pitch of 500, 1000, and 1500 nm with a planar device as control sample. Indeed, the hematite-deposited NSP device shows much better light absorption than the planar one, especially for longer wavelength, indicating strong light trapping effect with NSPs. Notably, among three different pitches, NSPs with pitch of 500 and 1000 nm have marginal difference and they are both much better than that of 1500 nm pitch. Interestingly, it seems 1000 nm pitch NSPs (Figure 2e) have much higher aspect ratio than the 500 nm pitch NSPs (Supporting Information Figure S7) after multiple layers deposition, however their optical absorption is close to each other. This can be explained by the two-fold facts. The 1000 nm pitch NSPs have high aspect ratio that leads to enhanced light scattering in the array and decent light absorption as well. Meanwhile, as 500 nm pitch is comparable to the incident wavelength, the diffraction effect can help to achieve high

optical absorption as well.<sup>31</sup> Since the 1000 nm pitch NSPs have large tunability on NSP height, systematic investigation on NSP height dependent light absorption was also carried out. Figure 3b shows the optical absorption spectra of devices with NSP height of about 350, 750, and 1100 nm, and it is conspicuous that optical absorption increases monotonically with NSP height that can be attributed to the improved light scattering by taller NSP structure with higher aspect ratio.

Besides optical measurements performed with experiments, finite-difference-time-domain (FDTD) simulations have also been performed to verify the experimental results. Figure 3c shows air mass 1.5 global (AM 1.5G) spectrum integrated absorption of NSP samples within the wavelength range 300–600 nm as the band gap of hematite is  $\sim 2.1$  eV with different combination of heights and pitches. The results clearly show that the NSP array architecture can trap light efficiently, as

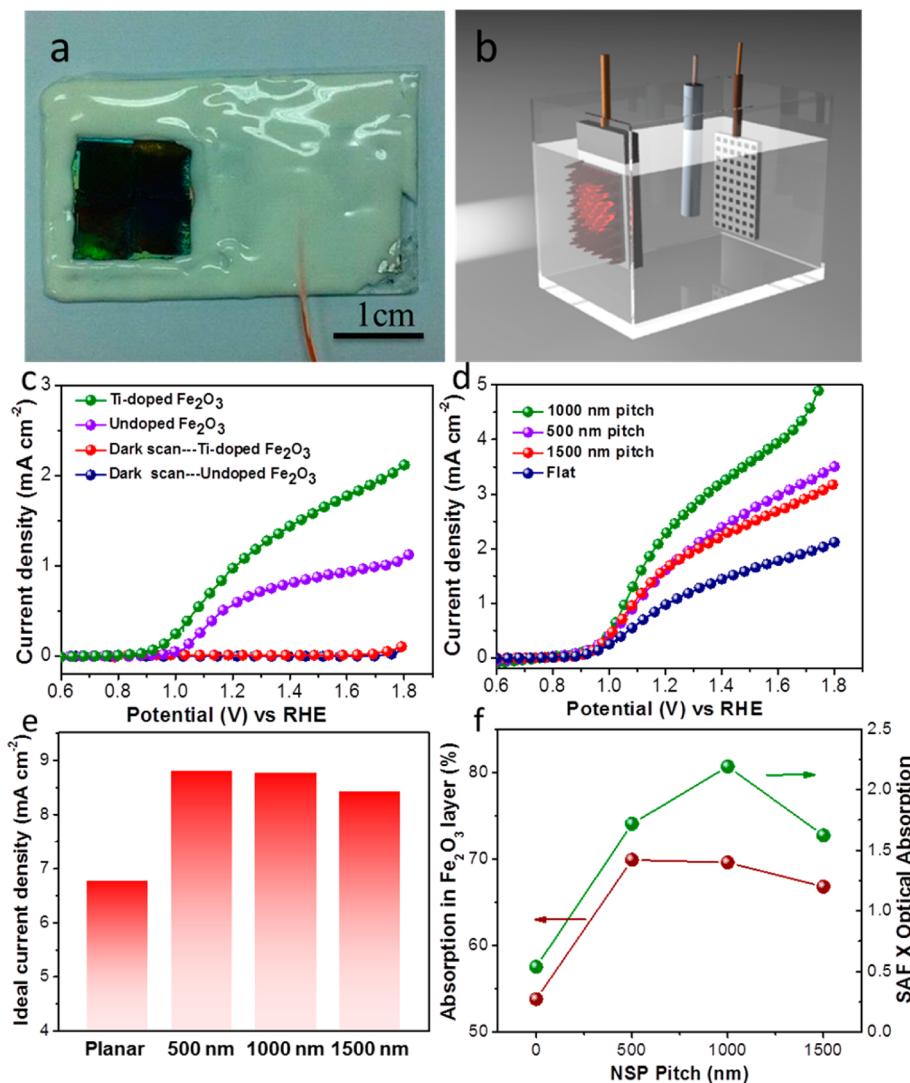


**Figure 4.** Photoelectrochemical test. (a) An optical image of the Ti-doped Fe<sub>2</sub>O<sub>3</sub> decorated NSP photoelectrode. (b) Schematic diagram showing a three-electrode configuration for water splitting test. (c)  $J$ - $V$  curves of the undoped hematite photoelectrode and the Ti-doped hematite photoelectrode obtained in 1 M NaOH solution (pH 13.6) and at 20 mV S<sup>-1</sup> scan rate. The corresponding dark currents are also shown. (d)  $J$ - $V$  curves of the Ti-doped hematite photoelectrodes based on the three different NSP arrays, showing the best performance achieved with the 3D NSP array photoelectrode with a pitch of 1000 nm. (e) Ideal current density of planar and the tallest NSP in different pitches calculated by simulated absorption in Fe<sub>2</sub>O<sub>3</sub> layer. (f) Plot of simulated absorption in Fe<sub>2</sub>O<sub>3</sub> layer (left y-axis) and its product with surface area factor (right y-axis).

revealed by the comparison with the planar control sample. In particular, three different NSP heights that are 35%, 75%, and 110% of the NSP pitch were chosen for FDTD simulation of optical absorption. In brief, it is concluded that optical absorption increases with NSP height and with the best absorption of 95.9% for 1000 nm pitch NSP array and 94.2% for 500 nm pitch NSP array. The trends of the simulation results agree well with that of the experiments. Moreover, to further understand the microscopic details underlying the superior light trapping capability of NSP substrate over the planar control, the simulated cross-sectional photon absorption distribution profile corresponding to wavelength range 300–600 nm of devices on planar and tall NSP are presented in Figure 3d1,d2 respectively. The red color hot area in Fe<sub>2</sub>O<sub>3</sub> representing high photon absorption on NSP substrate is much greater than that on planar substrate, which reveals the significant light trapping enhancement by using the 3D NSP photoelectrode. In addition, it is worth pointing out that high absorption can be found around the tip of the NSP, part of the

side wall, and around the valley between the neighboring NSPs. This is in fact a rather even distribution of the high absorption region and highly preferable for efficient PEC water splitting, due to the low rate constant of water oxidation and a short hole diffusion length. However, even distribution of light absorption can not necessarily be obtained with other hierarchical and complex structures.<sup>18</sup> The excellent light-harvesting property of the NSP structures is certainly highly preferable for solar energy conversion devices, such as solar photovoltaic cells and solar water splitting devices. In this work, photoelectrochemical experiments on the 3D NSP devices with ultrathin hematite films have been performed. An optical image of a Ti-doped hematite decorated NSPs photoelectrode is shown in Figure 4a. The performance was characterized by using a three-electrode electrochemical cell configuration for PEC water splitting tests, where the Ti-doped  $\alpha$ -Fe<sub>2</sub>O<sub>3</sub> deposited on the 3D spiked substrates as the working electrode, a platinum coil as the counter electrode, and Ag/AgCl as the reference electrode (Figure 4b). Figure 4c,d show a set of linear-sweep voltammo-

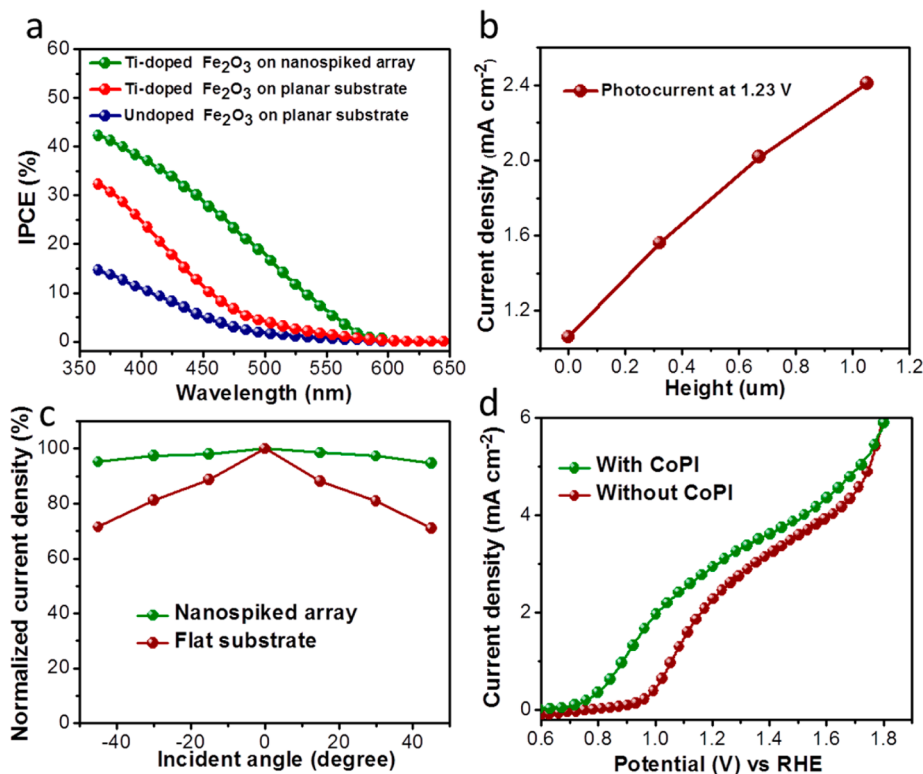


**Figure 5.** Photoelectrochemical test. (a) The corresponding IPCE measurements at 1.23 V versus RHE. (b) Photocurrent as a function of height at 1.23 V versus RHE. (c) Comparison of the angular dependence of photocurrent between the planar substrate and the NSP substrate, showing only a slight decrease in photocurrent for the latter in going from 0 to 45° irradiation. (d) Comparison of the  $J$ - $V$  curves between the Ti-doped  $\text{Fe}_2\text{O}_3$  with CoPI and without CoPI, showing the cathodic shift after CoPI coating.

grams (reported with respect to the reversible hydrogen electrode (RHE),  $E(\text{RHE}) = E(\text{Ag}/\text{AgCl}) + 0.1976 \text{ V} + 0.059 \text{ pH}$ ) recorded on different thin films under illumination of simulated sunlight (AM 1.5,  $100 \text{ mW}/\text{cm}^2$ ). Specifically, Figure 4c shows the results from planar samples with Ti-doped and undoped  $\alpha\text{-Fe}_2\text{O}_3$  deposited NSPs, upon sweeping the potential from 0.6 to 1.8 V vs RHE under illumination. It can be clearly seen that the Ti-doped  $\alpha\text{-Fe}_2\text{O}_3$  deposited on the planar substrate showed a photocurrent density of  $1.05 \pm 0.01 \text{ mA cm}^{-2}$  at 1.23 V vs RHE, which is about 1.75 times that of the undoped one. The enhancement is ascribed to over 2 orders of magnitude increase in the donor density of  $\text{Fe}_2\text{O}_3$  (Supporting Information Figure S8). Notably, the Ti-doped  $\alpha\text{-Fe}_2\text{O}_3$  deposited on the NSP substrates with three different pitches shows significant photocurrent enhancement from the planar configuration. The photocurrent density for the 1000 nm pitched electrode is  $2.42 \pm 0.02 \text{ mA cm}^{-2}$  at 1.23 V versus RHE, which is much higher than those with pitches of 500 nm ( $1.75 \pm 0.01 \text{ mA cm}^{-2}$ ) and 1500 nm ( $1.74 \pm 0.01 \text{ mA cm}^{-2}$ ) at the same applied potential. Note that this photocurrent is among the highest achieved with hematite without further water oxidation catalytic treatment.<sup>10,36,37</sup> Upon further potential increase, it can ramp up to  $3.96 \pm 0.03 \text{ mA cm}^{-2}$  at 1.60 V versus RHE. The optical measurements and modeling in Figure 3 have shown that the absorption of the 500 nm pitch NSPs and 1000 nm NSPs have marginal difference, however, their PEC photocurrent in Figure 4d is conspicuously different. This fact indicates that light absorption is not the only determining factor for a PEC process. To further shed light on the underlying mechanism, the photon absorption in the active hematite film only was integrated volumetrically leading to ideal

photocurrent shown in Figure 4e. Interestingly, the 500 nm pitch NSPs show the highest photocurrent of  $8.81 \text{ mA cm}^{-2}$ , followed by 8.77 and  $8.42 \text{ mA cm}^{-2}$  for 1000 and 1500 nm pitch NSPs, respectively, while the planar device only has an ideal current of  $6.78 \text{ mA cm}^{-2}$ . As the ideal photocurrent is  $12.6 \text{ mA cm}^{-2}$  for hematite, the percentage absorption in the active layer was calculated and shown in Figure 4f (the red color dot line). Furthermore, as the water oxidation process is slow, large surface area of the photoelectrode is highly preferable. In fact, a surface-area-factor (SAF) has been defined as ratio between the actual total photoanode surface area and the planar photoanode area with the same size. Supporting Information Figure S9 plots the SAF versus NSP pitches for the tallest structures in each pitch. It can be clearly seen that by definition the planar electrode has SAF of 1.0, and the 1000 nm pitch NSP electrode has the highest SAF of 3.15 as opposed to 2.46 and 2.43 for 500 and 1500 nm pitch NSP electrodes. Even though 500 nm pitch NSPs have much smaller aspect ratio than that of the 1500 nm pitch NSPs, the former has much higher NSP density, leading to a comparable SAF with the latter. As both the light absorption and electrode surface area are critical, the product of SAF and percentage optical absorption in the hematite is plotted in Figure 4f (the green dot line). Intriguingly, the trend of the product is in perfect consistency with the photocurrent trend shown in Figure 4d. Namely, the 1000 nm pitch NSP electrode yields the highest photocurrent and the 500 nm pitch NSP electrode slightly outperform the 1500 nm pitch NSP electrode. These results clearly show that the determining factors of the PEC performance of a photoelectrode include both light absorption capability and the photoanode surface area. Meanwhile, it is noteworthy that this conclusion is valid

based on the assumption that the light absorption profile is rather uniformly distributed across the entire device. In the case that there are localized “hot spots” of light absorption, the large surface area of the electrode may not be effectively utilized simply due to the lack of photocarrier generation elsewhere. In fact, this understanding couples light absorption, carrier collection, and surface area together which has not been systematically revealed before, and it can provide rational design guidelines for high performance PEC devices.

To further shed light on the PEC enhancement, incident photon-to-electron conversion efficiency (IPCE) measurements were performed on the different types of photoelectrodes at 1.23 V vs RHE. The results are shown in Figure 5a. First of all, compared to the undoped  $\text{Fe}_2\text{O}_3$  on the planar substrate the optimized Ti-doped  $\alpha\text{-Fe}_2\text{O}_3$  on the planar substrate exhibits significantly enhanced IPCE over the whole wavelength range from 365 to 600 nm, which is consistent with the  $J$ - $V$  measurements shown in Figure 4c. And this observation also suggests the improved carrier collection efficiency after Ti doping. Meanwhile, the Ti-doped  $\alpha\text{-Fe}_2\text{O}_3$  on the NSP substrate shows much higher IPCE than both Ti-doped  $\alpha\text{-Fe}_2\text{O}_3$  and undoped  $\alpha\text{-Fe}_2\text{O}_3$  on the planar substrates at the same wavelength. For example, the IPCE of Ti-doped  $\text{Fe}_2\text{O}_3$  deposited on the NSP substrate with a pitch of 1000 nm is 18.0% at 500 nm, which is much higher than 4.1% of Ti-doped  $\text{Fe}_2\text{O}_3$  and 1.7% of undoped  $\text{Fe}_2\text{O}_3$  on the planar substrates at the same wavelength. This fact is consistent with the optical measurement results shown in Figure 3a and it clearly demonstrates the largely improved photon capturing capability with the NSP architecture. Furthermore, we have found that the PEC efficiency has a monotonic dependence on the height of NSP arrays as well. Figure 5b shows the photocurrent of NSP devices with 1000 nm pitch at 1.23 V vs RHE, as a function of the height of NSPs. Clearly, with the increase in height the Ti-doped hematite NSP devices show photocurrent density increase from  $1.05 \pm 0.01 \text{ mA cm}^{-2}$  for “0” height (planar device) to  $2.42 \pm 0.02 \text{ mA cm}^{-2}$  with the largest NSP height, confirming the optical measurement results shown in Figure 3b. Meanwhile, this result also suggests that by further increasing the height of NSPs, even higher photocurrent can be obtained in the future with the device fabrication scheme reported here. The above measurements have been performed with normal incident light. However, scenarios with oblique angle light incident need to be considered from a practical perspective, since the sunlight incident angle varies in a day. In this regard, photocurrent of a device was measured at different light incident angle, then normalized to the light projection area to achieve current density. As shown in Figure 5c, the current density for the 3D NSP device only dropped by 3.5% with the largest irradiation angle ( $45^\circ$ ), as a comparison, the current density loss is as high as 28.5% for the planar device. These results suggest the 3D NSP structures have omnidirectional light-harvesting capability that is highly attractive for practical applications. Meanwhile, because cobalt phosphate (CoPI) is a good water oxidation catalyst, we employed it to cathodically shift the photocurrent curve.<sup>38–40</sup> As shown in Figure 5d, after electrodeposition of CoPI onto the 3D photoelectrode a much higher photocurrent density of  $3.05 \pm 0.03 \text{ mA cm}^{-2}$  was achieved at 1.23 V versus RHE, which continued to rise up to  $4.36 \pm 0.03 \text{ mA cm}^{-2}$  at 1.60 V versus RHE. To our best knowledge, this result represents by far the highest current density as compared with other ultrathin hematite photoelectrode reported.<sup>10,36,37</sup> Also, further PEC

performance enhancement is possible by improving, for example, the hematite deposition on taller NSP arrays.

In conclusion, we have demonstrated a unique and scalable fabrication process of regular arrays of nanospikes with precisely controlled periodicity and aspect ratio. Such 3D architectures have been used as photoelectrodes in conjunction with ultrathin hematite films coated atop. Our experiments and modeling results have shown that the 3D nanophotonics electrodes can significantly enhance photon-capturing capability omnidirectionally as well as photoanode surface area, leading to a high photocurrent density with ultrathin hematite films. The findings in this work suggest the rational design guidelines of high performance PEC. Namely, the factors of optical absorption profile, carrier collection efficiency, and actually electrode surface area need to be put into consideration for performance optimization. The significant advancement demonstrated here suggests that the purpose-built 3D NSP arrays are highly promising photoelectrodes for efficient PEC water splitting and further structural nanoengineering may lead to more performance boost in the future.

## ■ ASSOCIATED CONTENT

### Supporting Information

Materials and methods, Figures S1–S9. This material is available free of charge via the Internet at <http://pubs.acs.org>.

## ■ AUTHOR INFORMATION

### Corresponding Authors

\*E-mail: (Z.F.) [eezfan@ust.hk](mailto:eezfan@ust.hk).

\*E-mail: (S.Y.) [chsyang@ust.hk](mailto:chsyang@ust.hk).

### Author Contributions

Y.Q., S.-F.L., Z.F., and S.Y. designed and led the project. S.-F.L. fabricated 3D NSP Al substrate. Z.W. contributed to the USP preparation. Q.Z., B.H., and S.-F.L. contributed to the FDTD simulations. S.-F.L., Y.Q., Z.F., and S.Y. cowrote the paper. All the authors discussed the results and commented on the manuscript.

Y.Q. and S.-F.L. contributed equally to this work.

### Notes

The authors declare no competing financial interest.

## ■ ACKNOWLEDGMENTS

This work was supported by General Research Fund (612111, 612113, 606511, and 605710) from Hong Kong Research Grant Council. We also acknowledge National Research Foundation of Korea (NRF-2011-001496, 2008-066225).

## ■ REFERENCES

- (1) Lewis, N. S.; Nocera, D. G. *Proc. Natl. Acad. Sci. U.S.A.* **2006**, *43*, 15729–15735.
- (2) Grätzel, M. *Nature* **2001**, *6861*, 338–344.
- (3) Bard, A. J.; Fox, M. A. *Acc. Chem. Res.* **1995**, *3*, 141–145.
- (4) Nocera, D. G. *Acc. Chem. Res.* **2012**, *5*, 767–776.
- (5) Dotan, H.; Kfir, O.; Sharlin, E.; Blank, O.; Gross, M.; Dumchin, I.; Ankonina, G.; Rothschild, A. *Nat. Mater.* **2012**, 158–164.
- (6) Jia, Q.; Iwashina, K.; Kudo, A. *Proc. Natl. Acad. Sci. U.S.A.* **2012**, *29*, 11564–11569.
- (7) Reece, S. Y.; Hamel, J. A.; Sung, K.; Jarvi, T. D.; Esswein, A. J.; Pijpers, J. J.; Nocera, D. G. *Science* **2011**, *6056*, 645–648.
- (8) Qiu, Y.; Yan, K.; Deng, H.; Yang, S. *Nano Lett.* **2011**, *1*, 407–413.
- (9) Barroso, M.; Mesa, C. A.; Pendlebury, S. R.; Cowan, A. J.; Hisatomi, T.; Sivula, K.; Graetzel, M.; Klug, D. R.; Durrant, J. R. *Proc. Natl. Acad. Sci. U.S.A.* **2012**, *39*, 15640–15645.

- (10) Sivula, K.; Le Formal, F.; Graetzel, M. *ChemSusChem* **2011**, *4*, 432–449.
- (11) Ling, Y.; Wang, G.; Wheeler, D. A.; Zhang, J. Z.; Li, Y. *Nano Lett.* **2011**, *5*, 2119–2125.
- (12) Wang, G.; Ling, Y.; Wheeler, D. A.; George, K. E. N.; Horsley, K.; Heske, C.; Zhang, J. Z.; Li, Y. *Nano Lett.* **2011**, *8*, 3503–3509.
- (13) Tilley, S. D.; Cornuz, M.; Sivula, K.; Grätzel, M. *Angew. Chem., Int. Ed.* **2010**, *36*, 6549–6552.
- (14) Warren, S. C.; Voitchovsky, K.; Dotan, H.; Leroy, C. M.; Cornuz, M.; Stellacci, F.; Hebert, C.; Rothschild, A.; Graetzel, M. *Nat. Mater.* **2013**, *9*, 842–849.
- (15) Kennedy, J. H.; Frese, K. W. *J. Electrochem. Soc.* **1978**, *5*, 709–714.
- (16) Cho, I. S.; Logar, M.; Lee, C. H.; Cai, L.; Prinz, F. B.; Zheng, X. *Nano Lett.* **2014**, *1*, 24–31.
- (17) Mohapatra, S. K.; John, S. E.; Banerjee, S.; Misra, M. *Chem. Mater.* **2009**, *14*, 3048–3055.
- (18) Kay, A.; Cesar, I.; Graetzel, M. *J. Am. Chem. Soc.* **2006**, *49*, 15714–15721.
- (19) Kim, J. Y.; Magesh, G.; Youn, D. H.; Jang, J.; Kubota, J.; Domen, K.; Lee, J. S. *Sci. Rep.* **2013**, *3*, 2681–2688.
- (20) Zhu, J.; Yin, Z.; Yang, D.; Sun, T.; Yu, H.; Hoster, H. E.; Hng, H. H.; Zhang, H.; Yan, Q. *Energy Environ. Sci.* **2013**, *3*, 987–993.
- (21) Xu, Y.; Gao, M.; Zheng, Y.; Jiang, J.; Yu, S. *Angew. Chem., Int. Ed.* **2013**, *33*, 8546–8550.
- (22) Lin, Y.; Battaglia, C.; Boccard, M.; Hettick, M.; Yu, Z.; Ballif, C.; Ager, J. W.; Javey, A. *Nano Lett.* **2013**, *11*, 5615–5618.
- (23) Yin, H.; Zhao, S.; Wan, J.; Tang, H.; Chang, L.; He, L.; Zhao, H.; Gao, Y.; Tang, Z. *Adv. Mater.* **2013**, *43*, 6270–6276.
- (24) Cheng, Q.; Wu, M.; Li, M.; Jiang, L.; Tang, Z. *Angew. Chem., Int. Ed.* **2013**, *13*, 3838–3843.
- (25) Wang, J.; Cheng, Q.; Tang, Z. *Chem. Soc. Rev.* **2012**, *3*, 1111–1129.
- (26) Stefik, M.; Cornuz, M.; Mathews, N.; Hisatomi, T.; Mhaisalkar, S.; Graetzel, M. *Nano Lett.* **2012**, *10*, 5431–5435.
- (27) Chiang, C.; Epstein, J.; Brown, A.; Munday, J. N.; Culver, J. N.; Ehrman, S. *Nano Lett.* **2012**, *11*, 6005–6011.
- (28) Sivula, K.; Formal, F. L.; Grätzel, M. *Chem. Mater.* **2009**, *13*, 2862–2867.
- (29) Hisatomi, T.; Dotan, H.; Stefik, M.; Sivula, K.; Rothschild, A.; Graetzel, M.; Mathews, N. *Adv. Mater.* **2012**, *20*, 2699–2702.
- (30) Yu, R.; Ching, K.; Lin, Q.; Leung, S.; Arcrossito, D.; Fan, Z. *ACS Nano* **2011**, *11*, 9291–9298.
- (31) Leung, S. F.; Yu, M.; Lin, Q.; Kwon, K.; Ching, K. L.; Gu, L.; Yu, K.; Fan, Z. *Nano Lett.* **2012**, *12*, 3682–3689.
- (32) Fan, Z. Y.; Razavi, H.; Do, J. W.; Moriwaki, A.; Ergen, O.; Chueh, Y. L.; Leu, P. W.; Ho, J. C.; Takahashi, T.; Reichertz, L. A.; Neale, S.; Yu, K.; Wu, M.; Ager, J. W.; Javey, A. *Nat. Mater.* **2009**, *8*, 648–653.
- (33) Lin, Q.; Leung, S.; Tsui, K.; Hua, B.; Fan, Z. *Nanoscale Res. Lett.* **2013**, *1*, 268.
- (34) Deceglie, M. G.; Ferry, V. E.; Alivisatos, A. P.; Atwater, H. A. *Nano Lett.* **2012**, *6*, 2894–2900.
- (35) Battaglia, C.; Hsu, C.; Söderström, K.; Escarré, J.; Haug, F.; Charrière, M.; Boccard, M.; Despeisse, M.; Alexander, D. T. L.; Cantoni, M.; Cui, Y.; Ballif, C. *ACS Nano* **2012**, *3*, 2790–2797.
- (36) Li, Z.; Luo, W.; Zhang, M.; Feng, J.; Zou, Z. *Energ. Environ. Sci.* **2013**, *2*, 347–370.
- (37) Lin, Y.; Yuan, G.; Sheehan, S.; Zhou, S.; Wang, D. *Energy Environ. Sci.* **2011**, *12*, 4862–4869.
- (38) Kanan, M. W.; Nocera, D. G. *Science* **2008**, *5892*, 1072–1075.
- (39) Zhong, D. K.; Sun, J.; Inumaru, H.; Gamelin, D. R. *J. Am. Chem. Soc.* **2009**, *17*, 6086–6087.
- (40) Zhong, D. K.; Gamelin, D. R. *J. Am. Chem. Soc.* **2010**, *12*, 4202–4207.